JOURNAL OF GEOPHYSICAL RESEARCH, VOL. 93, NO. C12, PAGES 15,427–15,436, DECEMBER 15, 1988

On the Time-Averaged Flow of Quasi-Geostrophic Wind-Driven Gyres

J. C. MARSHALL, A. J. G. NURSER, AND R. BRUGGE

Space and Atmospheric Physics Group, Department of Physics, Imperial College, London

The time-averaged flow of a three-layer eddy-resolving quasi-geostrophic ocean model is considered in the light of two analytical models of wind-driven gyres, in which the vertical structure of the gyre is set by assuming that potential vorticity is uniform beneath layers exposed to forcing. The first, due to Young and Rhines (1982), supposes that the depth-integrated meridional transport is set by the imposed wind-stress curl. In contrast, in the baroclinic Fofonoff gyres of Marshall and Nurser (1986, 1988), inertial aspects of the flow are emphasized without imposing a Sverdrup constraint. The mean fields from the model are seen to lie between the two extremes represented by these analytical solutions. In the interior of the gyre away from inertial boundary currents and jets, the Sverdrup constraint is obeyed, and the mean flows resemble the Young and Rhines solution. However, the essential character of the overspun recirculation, including the weakly depth-dependent nature of the currents in its return flow, seem to be well captured in the inertial limit considered by Marshall and Nurser.

1. INTRODUCTION

The canonical studies of *Stommel* [1948] and *Fofonoff* [1954] provided firm reference points for subsequent numerical studies based on the barotropic vorticity equation [*Bryan*, 1963; *Veronis*, 1966]. In the present article we point out that logical extensions to a baroclinic ocean of the Stommel and Fofonoff barotropic solutions are provided by, respectively, the *Young and Rhines* [1982] and *Marshall and Nurser* [1986, 1988] studies (hereinafter YR and MN respectively). These analytical solutions represent useful limit cases from which to contemplate the mean flows found in baroclinic eddy-resolving quasi-geostrophic numerical models.

YR consider the limit in which the depth-integrated transport is set by the imposed wind stress curl. Below the surface layers it is supposed (following *Rhines and Young* [1982]) that in regions shielded from forcing in which there is motion, the potential vorticity becomes homogenized to a uniform value. Instead, MN exploit this idea in the inertial limit and obtain baroclinic Fofonoff gyres which are not constrained by Sverdrup balance. Our purpose here is to demonstrate, by direct comparison with a numerical integration, that the models (and by implication, perhaps, the ocean) lie somewhere between the limit cases represented by these analytical theories. In section 2, time-averaged fields from a wind-driven three-layer quasi-geostrophic numerical model are presented. These mean flows are considered in the light of the YR solution (section 3) and the MN solution (section 4).

2. THE TIME-AVERAGED FIELDS

Figure 1 shows the time-average (a 3-year time-average of the statistically steady state) streamfunction and potential vorticity from a three-layer quasi-geostrophic eddy-resolving model driven by an antisymmetric wind stress curl and retarded by bottom friction. Details of the model can be found in the appendix.

Paper number 88JC03234.
0148-0227/88/88JC-03234$05.00

The upper level flow (Figure 1*a*) shows a familiar double gyre: a concentrated jet penetrates halfway across the basin along the zero wind stress curl line and diminishes to join on to the Sverdrupian interior. The mean gyres strongly deform the potential vorticity (q) field. Associated with the interior jet there is a strong front in the q field, (Figure 1*d*), where relative vorticity makes an important contribution. Away from the jet vortex, stretching allows the q contours to fan out; some turn back on themselves and close off, and others attach themselves at their reference latitudes on the eastern coast.

In the middle layer (Figure 1*e*), we see the homogenized pool of potential vorticity which is so characteristic of this genre of model. In contrast to the upper level where an antisymmetric wind stress curl maintains a front in the q field along the zero-curl line, in the middle layer (shielded from external forcing) the q contours have been expelled to the north and south. *Rhines and Young* [1982] attribute this plateau in the q field to the effect of the eddy field smoothing out q gradients. Strong flow in the layer is confined to this homogenized region: despite the uniformity of q the flow here is strongly constrained by the pattern of upper layer flow. It again exhibits an inertial character with a narrow jet at mid-basin recirculating to the north and south (Figure 1*b*).

In the third layer, bottom friction prevents the complete smoothing of the q field, but again, gradients of q are less marked in the regions of strong flow (Figure 1*f*). Flow is confined to a region of restricted meridional extent and exhibits two counter-rotating gyres close to the axis of the free jet at midbasin (Figure 1*c*). Here, where flow extends through the whole depth of the ocean, there is a barotropic (depth-independent) component confined to the recirculation on either side of the eastward flowing jet: the flow in layer three is the signature of this depth-independent component.

The general characteristics exhibited in Figure 1 are found over a wide range of model parameters, and so can be considered to be rather robust features of this wind-driven model. Comparison of such models with observations reported by *Schmitz and Holland* [1986], suggests that gross features of the recirculation, both in its mean and eddy statistics, are represented. However, the degree of to which advection controls the character of the circulation is sensitive to model pa-

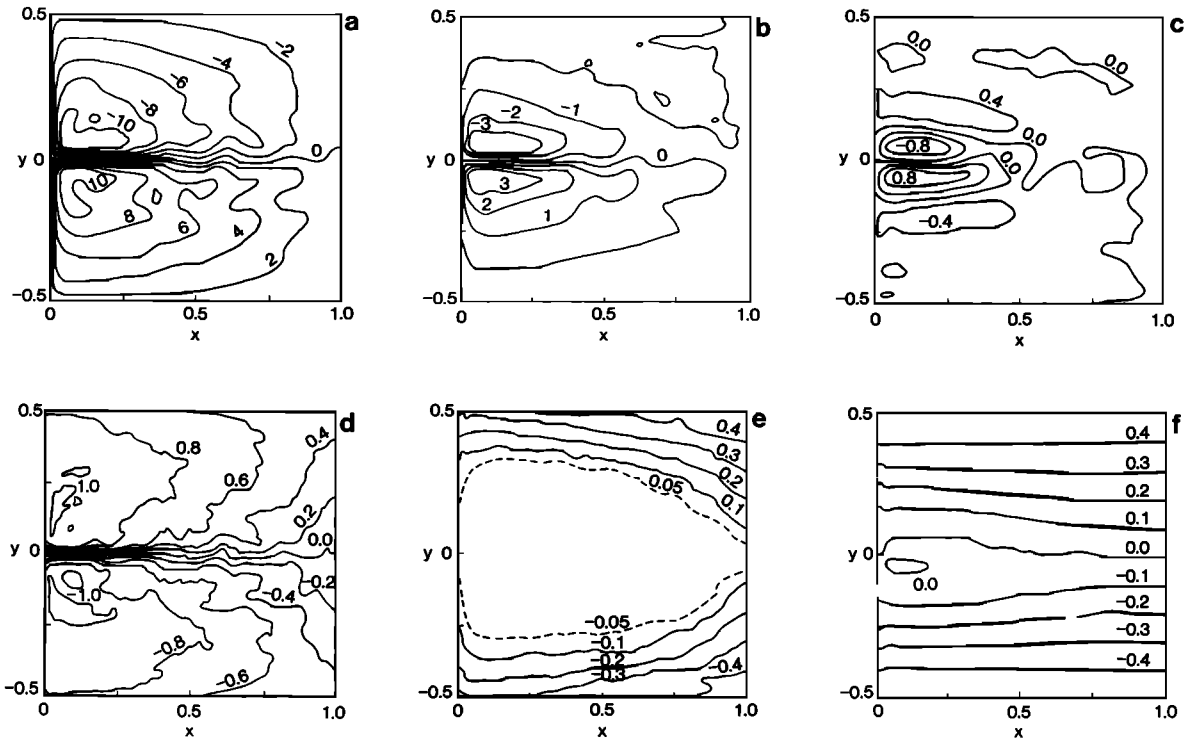

Fig. 1. The time-mean fields (nondimensionalized) from the three-layer integration described in the appendix for streamfunction (*a*) ψ_1, (*b*) ψ_2, (*c*) ψ_3 and potential vorticity (*d*) q_1, (*e*) q_2, (*f*) q_3.

rameters: the penetration scale of the jet is a complicated function of the (mixed) instability of the free jet which is sensitive to explicit diffusion, vertical resolution, layer depth and stratification [see *Holland and Schmitz*, 1985]. The inertial limit, in which the jet penetrates all the way across the basin along the zero-curl line, is difficult to achieve owing to the instability of the free jet. However, the mean flow of Figure 1 is substantially greater than the Sverdrup transport with the jet penetrating almost halfway across the basin; the transport streamfunction plotted in Figure 2 shows that the circulation of the gyre exceeds the Sverdrup transport by a factor of about 2.5, with a substantial fraction being associated with the weakly depth-dependent recirculation of which the lower layer flow is a signature; compare Figure 1*c* with Figure 2. This weakly depth-dependent return flow is also a feature of the observations [see *Schmitz*, 1980].

3. The YR Model

YR considered a two-layer extension of the *Stommel* [1948] model; here a straightforward development to three layers is presented for comparison with the numerical model of section 2. The details of the frictional boundary layers are considered by *Ierley and Young* [1983] but are not studied here.

It is supposed that the depth-integrated flow is in Sverdrup balance (all symbols are defined in the appendix)

$$\psi_B = \int_{x=1}^{x} W_o \, dx = (1-x)\sin 2\pi y \qquad (1)$$

where

$$\psi_B = \delta_1\psi_1 + \delta_2\psi_2 + \delta_3\psi_3$$

is the barotropic streamfunction and equation (A5) has been used.

The balance of terms in the potential vorticity equation for each of the layers is assumed to be (away from frictional boundary layers)

$$J(\psi_1, q_1) = W_o/\delta_1 \qquad (2a)$$

$$J(\psi_2, q_2) = 0 \qquad (2b)$$

$$J(\psi_3, q_3) = 0 \qquad (2c)$$

where the values of q are given by (A2) and (A3) in the appendix but with the relative vorticity neglected.

Equations (2*b*) and (2*c*) imply that q is constant along streamlines. *Rhines and Young* [1982], in an application of the Prandtl-Batchelor theorem (see also *Niiler* [1966]),

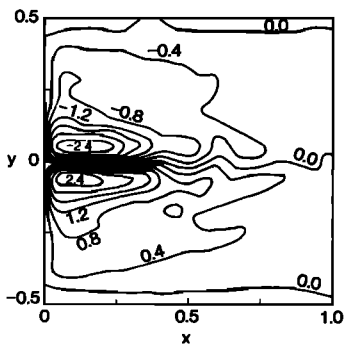

Fig. 2. The time-mean depth-integrated streamfunction from the three-layer integration described in the appendix, $\psi_B = \delta_1\psi_1 + \delta_2\psi_2 + \delta_3\psi_3$.

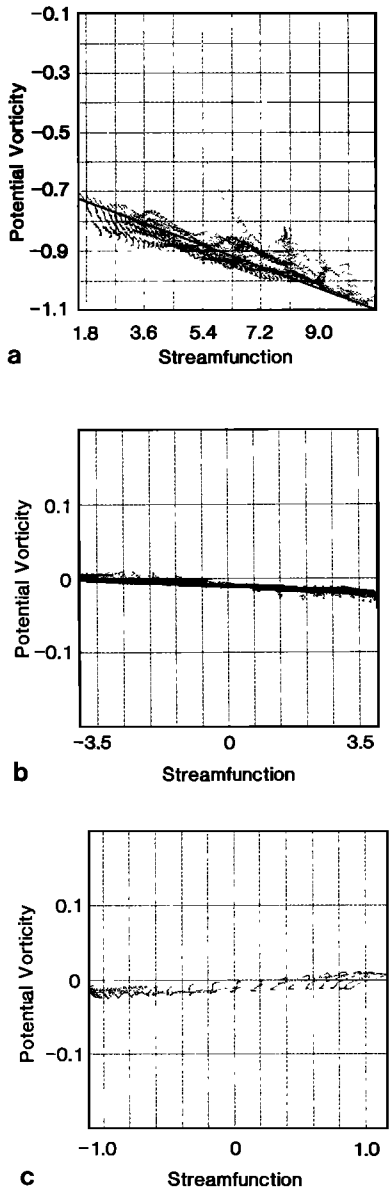

Fig. 3. Scatter diagrams of q against ψ. (*a*) Layer 1 over the subtropical recirculation (excluding boundary currents) $0.05 < x < 0.5$, $-0.5 < y < -0.15$. (*b*) Layer 2 over the homogenized pool $0.05 < x < 0.5$, $-0.15 < y < 0.15$. (*c*) Layer 3 over the deep recirculating gyres $0.05 < x < 0.3$, $-0.05 < y < 0.05$.

invoke integral balances between potential vorticity sources and sinks to constrain the functional relationship between q and ψ: they deduce that

$$\frac{dq_n}{d\psi_n} = \frac{-\int G_n \, dA}{\oint K_n U_n . dl} \tag{3}$$

where G_n is the potential vorticity forcing for the mean flow in each layer, K_n is a (positive) eddy transfer coefficient which parametrizes the transfer properties of the geostrophic eddy field, and U_n is the velocity around the circuit dl coincident with closed streamlines. Equation (3) assumes that over each gyre the lateral transfer by the geostrophic eddy field balances potential vorticity sources and sinks in each layer. Application of (3) to layers 2 and 3 allows one to deduce that if the eddies are strong, $dq_2/d\psi_2$ approaches zero from below whereas $dq_3/d\psi_3$ approaches zero from above [see MN, 1988]. Supporting evidence from the numerical model can be found in the scatter diagrams of q against ψ plotted for each layer in Figure 3. In layers 2 and 3, shielded from surface forcing, flow is confined to regions in which the q gradients are small; outside these regions q contours intersect the boundary, and so in the absence of forcing, the mean flow is weak and ψ is approximately constant.

In the YR model a flow regime as sketched in Figure 4 can be expected; in region I only the upper layer is in motion, and in region II only layers 1 and 2 are in motion, whereas in region III all three layers are in motion.

In region I the Sverdrup transport must be carried entirely by the upper layer and so

$$\begin{aligned} \psi_1 &= \psi_B/\delta_1 \\ \psi_2 &= \psi_3 = 0 \end{aligned} \tag{4}$$

The boundary between regions I and II is found by noting that the potential vorticity q_2 in the second layer is constant and equal to zero along this boundary (its value at $y = 0$).

Thus the boundary curve is given by

$$y + \frac{S_{21}\psi_B}{\delta_1} = 0 \tag{5}$$

In region II, where $\psi_3 = 0$ the Sverdrup transport is shared between layers 1 and 2,

$$\psi_B = \delta_1\psi_1 + \delta_2\psi_2 \tag{6a}$$

The partition of the transports betwen the layers can be found by noting that the potential vorticity in the second layer in region II is constant and equal to zero: thus

$$y + S_{21}\psi_1 - S_{22}\psi_2 = 0 \tag{6b}$$

Combining (6*a*) and (6*b*) leads to

$$\psi_1 = \frac{S_{22}\psi_B - \delta_2 y}{S_{22}\delta_1 + S_{21}\delta_2} \tag{7a}$$

$$\psi_2 = \frac{S_{21}\psi_B + \delta_1 y}{S_{22}\delta_1 + S_{21}\delta_2} \tag{7b}$$

$$\psi_3 = 0 \tag{7c}$$

Given the solution in region II the boundary between II and III can be found since q_3 is constant and equal to zero along this interface. The boundary curve is defined by

$$y + S_{32}\psi_2 = 0 \tag{8}$$

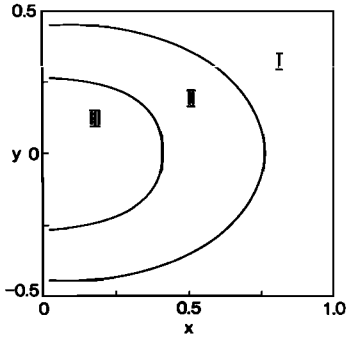

Fig. 4. Flow regime diagram for the YR model. In region I, only the upper layer is in motion; in region II, layers 1 and 2 are in motion, and in region III, all layers are in motion.

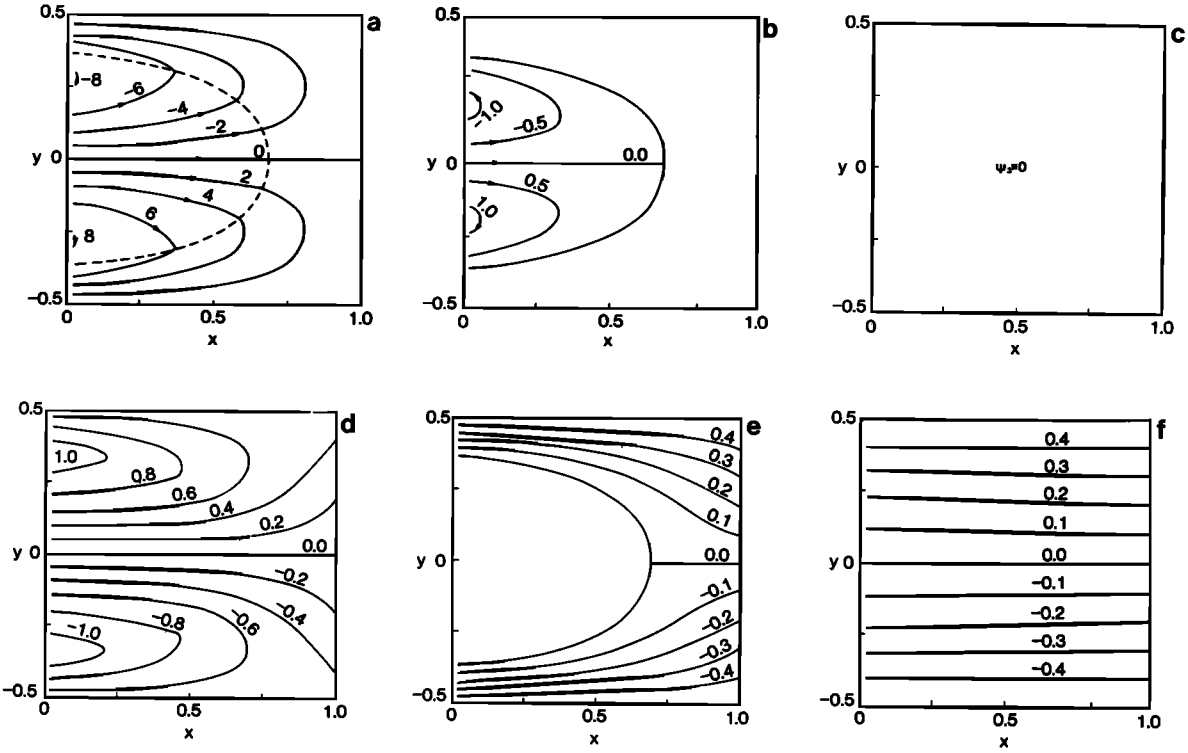

Fig. 5. The YR solution plotted from (4, 5, 7, 8 and 10) for the constants (A6) used in the numerical integration for streamfunction (*a*) ψ_1, (*b*) ψ_2, (*c*) ψ_3 and potential vorticity (*d*) q_1, (*e*) q_2, (*f*) q_3.

where ψ_2 is given by (7*b*). In region III, where all layers are in motion,

$$\begin{aligned} \psi_B &= \delta_1\psi_1 + \delta_2\psi_2 + \delta_3\psi_3 \\ q_2 &= y + S_{21}\psi_1 - S_{22}\psi_2 + S_{23}\psi_3 = 0 \\ q_3 &= y + S_{32}\psi_2 - S_{33}\psi_3 = C_3\psi_3 \end{aligned} \tag{9}$$

where C_3 is the positive constant $dq_3/d\psi_3$ which can be deduced empirically from Figure 3*c*.

Finally, solving (9) for ψ_1, ψ_2, ψ_3 gives

$$\psi_1 = D^{-1}\{(S_{22}C_3 + S_{21}S_{32})\psi_B - y[\delta_3(S_{22}+S_{32}) + \delta_2(C_3 + S_{32} + S_{23})]\} \tag{10a}$$

$$\psi_2 = D^{-1}\{(\delta_1 y + S_{21}\psi_B)(C_3 + S_{32}) - y(\delta_3 S_{21} - \delta_1 S_{23})\} \tag{10b}$$

$$\psi_3 = D^{-1}\{(\delta_1 y + S_{21}\psi_B)S_{32} + y(\delta_1 S_{22} + \delta_2 S_{21})\} \tag{10c}$$

where

$$D = (C_3 + S_{33})(\delta_1 S_{22} + \delta_2 S_{21}) + S_{32}(\delta_3 S_{21} - \delta_1 S_{23})$$

The streamfunction and potential vorticity are plotted in Figure 5 for the YR solution (equations (4), (5), (7), (8) and (10)), for the constants used in the numerical integration (see appendix, equation (A6)). Comparison with the numerical model (Figure 1) shows that this simple solution captures many of the broad features of the model mean fields. A particularly interesting aspect of the solution is the sweeping around of the q contours by the upper level flow in the westward return flow (Figures 5*a* and 5*d*). Although the upper layer is being directly driven by the wind, even here there is a tendency for the flow to align the ψ and q contours. This cannot occur in barotropic studies in which vortex stretching plays no role in contributing to the potential vorticity.

The horizontal extent of the region of homogenized q in the second layer is well captured in the YR solution, (Figure 5*e*). A closer inspection, however, reveals several deficiencies of the solution which can be traced back to the neglect of relative vorticity. In the upper layer (Figures 5*a* and 5*d*), eastward flow occurs in a broad current rather than as an intense jet. In fact, in the YR solution the maximum streamfunction occurs in the southern half of the subtropical gyre rather than in the northwestern corner as in the model. This absence of an inertial character is also evident in the q field: compare Figures 5*d* and 1*d*. Rather than bunching together along the zero wind stress curl line as in the numerical model, the q contours are widely spaced and lack a frontal structure.

The departure of the model from the YR solution is even more evident in the second and third layers. The YR solution (Figure 5*b*) grossly underestimates the transport in layer 2 and predicts no flow at all in the bottom layer; (8) cannot be satisfied. The depth-integrated circulation is limited by the Sverdrup constraint. In both of these layers of the numerical model; however, eastward flow occurs in inertial jets and recirculates to the north and south in the uniform pools of potential vorticity: the transport is not limited by the Sverdrup constraint. In fact, the depth-integrated circulation is overspun by a factor of 2.4 times the Sverdrup transport, with a significant fraction recirculating in a weakly depth-dependent return flow on either flank of the stream (see Figure 2).

4. THE MN MODEL

An extension of *Fofonoff*'s [1954] solution to a layered ocean governed by quasi-geostrophic dynamics is considered in *Marshall and Nurser* [1986, 1988]. Detailed calculations can be found in MN and will not be repeated here. However, an indication of how the calculation proceeds will be given.

Unlike the YR calculation, MN emphasize the homogeneous component of the flow which satisfies the unforced, undamped equations of motion; thus in place of (2) we have

$$J(\psi_n, q_n) = 0 \tag{11}$$

that is, q can be any constant value along streamlines. Again, following *Niiler* [1966] and *Rhines and Young* [1982], the ambiguities of the inviscid theory are removed by invoking integral balances between forcing and dissipation (the small terms that have been neglected on the right hand side of (11)) which serve to constrain the functional relationship as in (3).

Thus we have

$$q_1 = C_1\psi_1 + q_{10} \tag{12a}$$

$$q_2 = C_2\psi_2 \tag{12b}$$

$$q_3 = C_3\psi_3 \tag{12c}$$

where

$$q_{10} = 0.5, \qquad y > 0 \tag{12d}$$

$$q_{10} = -0.5 \qquad y < 0 \tag{12e}$$

is chosen to represent the sharp gradient in the q field at $y = 0$, and the C values are deduced from (3). It is this front in the upper layer q field which induces the gyres in the MN model. In the numerical model this frontal structure (Figure 1*d*) is a complicated function of the upper layer forcing and the instability of the eastward flowing jet. However, for analytical tractability, MN assume that q_{10} is independent of x, and so the solutions they obtain are of Fofonoff form and fill the gyre in the east-west direction. Other more realistic forms for q_{10} can be considered, but then solutions can be obtained only numerically.

As before, application of the circulation integral to each of the layers allows one to deduce that C_1 is negative and C_3 is positive, consistent with the scatter plots Figure 3. For analytical convenience we assume that $C_2 = 0$, i.e. that the q in the second layer is perfectly homogenized.

If (11) were satisfied exactly, then the points on the scatter plots (Figure 3) would collapse onto a line. That they do not implies that the advection terms do not vanish but balance sources and sinks. The degree of scatter is a measure of the magnitude of the advection terms or, alternatively, a measure of the coincidence of the q and ψ contours. In the upper layer, exposed to wind stress curl forcing, the points show considerable scatter although even here advective effects tend to align the q and ψ contours (compare Figures 1*a* and 1*d*). An estimate of the angle between between the q and ψ contours can be made from the scatter plots as follows.

Since

$$|\mathbf{v}_g.\nabla q| = |\nabla\psi||\nabla q|\sin\theta$$

the average angle θ over the gyre is given by

$$\sin\theta = \frac{1}{\Delta\psi\Delta q}\int \mathbf{v}_g.\nabla q\, dA \tag{13}$$

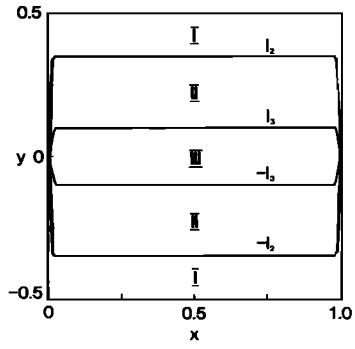

Fig. 6. Flow regime diagram for the MN solution.

where $\Delta q, \Delta\psi$ denotes the maximum range of q and ψ values in the scatter plot and, as was shown by *Read et al.* [1986], the integral is the area enclosed by the spread of points in the scatter diagram. MN use this angle as a small parameter in which to expand about the free solution, (equation (11)). Evaluation of the integral from Figure 3 gives a mean angle of only 15° in the upper layer.

In the MN model, C_1 and C_3 are assumed to be constants (i.e. the slopes of the q/ψ plots in Figure 3 are taken to be constant), and so the solutions found are generalizations of Fofonoff's solution. Away from boundary currents the flow must then be along latitude circles; the regime diagram has the form shown in Figure 6. The calculation proceeds as in section 2.

In region I, only the upper layer is in motion and away from the inertial boundary currents the solution is given by

$$\begin{aligned} \psi_1 &= (y - q_{10})/(C_1 + S_{11}) \\ \psi_2 &= \psi_3 = 0 \end{aligned} \tag{14}$$

As in section 2 the boundary between regions I and II is found by noting that the potential vorticity in the second layer is zero at this boundary. This, together with (14), enables one to deduce that these boundaries are at latitudes $y = \pm l_2$, where

$$l_2 = \frac{S_{21}q_{10}}{C_1 + S_{11} + S_{21}} \tag{15}$$

In region II, only the lower layer is at rest. It is straightforward to show that

$$\psi_1 = \frac{(S_{11} + S_{22})y - S_{22}q_{10}}{S_{22}C_1 + S_{11}S_{22} - S_{11}S_{21}} \tag{16a}$$

$$\psi_2 = \frac{S_{22}\left[(C_1 + S_{11} + S_{21})y - S_{21}q_{10}\right]}{S_{22}C_1 + S_{11}S_{22} - S_{11}S_{21}} \tag{16b}$$

$$\psi_3 = 0 \tag{16c}$$

Given the solution in region II, equation (16), the latitudes $y = \pm l_3$ separating II from III can be calculated, since the potential vorticity in the third layer must be zero at this boundary. It may be deduced that

$$l_3 = \frac{S_{32}S_{21}q_{10}}{C_1(S_{22} + S_{32}) + S_{11}(S_{22} + S_{32} - S_{21}) + S_{32}S_{21}} \tag{17}$$

In region III all three layers are in motion but note that l_3 itself does not depend on the details of the motion in region III: in particular, it is independent of C_3.

It should be noted that the prediction (17) for the meridional extent of the recirculatory flow in the third layer as-

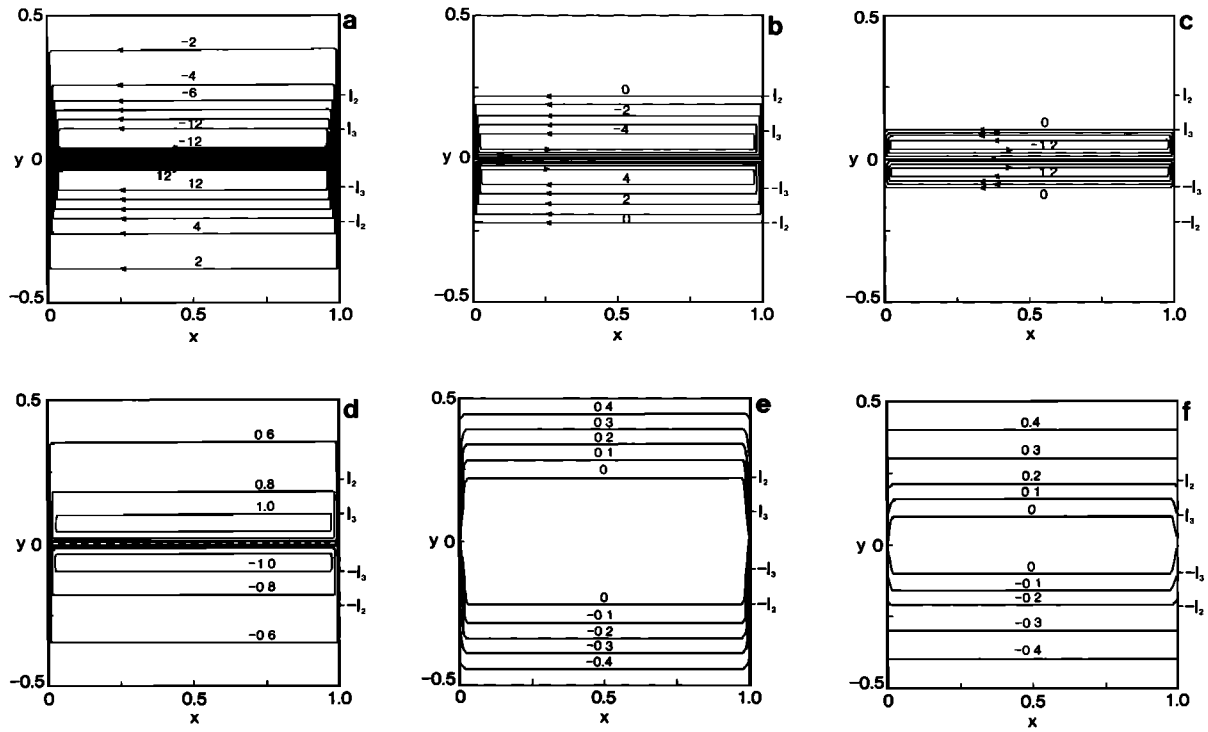

Fig. 7. The MN solution plotted from equations (14, 15, 16, 17 and 18) for the constants (equation (A6)) used in the numerical model for streamfunction (*a*) ψ_1, (*b*) ψ_2, (*c*) ψ_3 and potential vorticity (*d*) q_1, (*e*) q_2, (*f*) q_3. The functional relationships between q and ψ have been obtained by inspection of Figure 3 ($C_1 = -4\text{x}10^{-2}$, $C_3 = 1.2\text{x}10^{-2}$).

sumes continuity of the potential vorticity and hence vanishing of the relative vorticity at the edge of the deep gyre. This slippery boundary condition should be contrasted with the no-slip boundary condition applied by *Cessi et al.* [1987] in their barotropic inertial theory. Inspection of the mean fields from the numerical model (see Figure 1) strongly supports the slippery condition used by MN: the vorticity is zero, and the velocity is a maximum at the edge of the recirculating gyre in the lower layer. The relevance of the slippery boundary condition is also supported by the meridional sections which will be presented in section 5.

In region III the solution to the flow is the sum of a particular integral $\Psi_\mathbf{I}$, the interior solution satisfying

$$(\underline{\mathbf{S}}+\underline{\mathbf{C}})\Psi_\mathbf{I} = \mathbf{b} \qquad (18a)$$

and a complementary function or boundary correction $\Psi_\mathbf{B}$ satisfying

$$R\nabla^2\Psi_\mathbf{B} = (\underline{\mathbf{S}}+\underline{\mathbf{C}})\Psi_\mathbf{B} \qquad (18b)$$

where $\Psi_\mathbf{B} + \Psi_\mathbf{I} = 0$ at $y = 0$ and $\Psi_\mathbf{B} = 0$ at $y=\pm l_3$, again adopting a slippery boundary condition.

In (18) $\underline{\mathbf{S}}$ is the stretching matrix given by (A3),

$$\underline{\mathbf{C}} = \begin{pmatrix} C_1 & 0 & 0 \\ 0 & C_2 & 0 \\ 0 & 0 & C_3 \end{pmatrix}$$

is a diagonal matrix containing the functional relationships between q and ψ in each layer set by the circulation integrals (equation 3), and $\mathbf{b}$ is the source function

$$\mathbf{b} = \begin{pmatrix} y - q_{10} \\ y \\ y \end{pmatrix}$$

The complementary function is required to satisfy the boundary condition that ψ must be zero at $y = 0$, along the zero stress curl line at midbasin. It should be emphasized that relative vorticity plays a crucial role in the structure of both the eastward flowing jet at $y = 0$ and its recirculation to the north and south between the latitudes $y = \pm l_3$.

Explicit solutions to (18) for simple choices of $\underline{\mathbf{S}}$ and $\underline{\mathbf{C}}$ are given by MN [1988]: here it is sufficient to note that it comprises a depth-independent component, consequent upon the bowl of the circulation striking the ocean floor, together with a depth-dependent component considered by MN [1986]. For comparison with our three-layer model in which $\underline{\mathbf{S}}$ (equation (A3)) does not take a simple form, it was found convenient to solve (18) by numerical inversion.

The streamfunction and potential vorticity are plotted for the MN solution (equations (14), (15), (16), (17) and (18)) in Figure 7. Because of our choice of q_{10} (equation (12*b*)) the gyres fill the basin from east to west. A more notable aspect of the solution is its strong north-south asymmetry which is the signature of inertial effects. All eastward flow now occurs in an inertial jet; the meridional extent of the broader return flows to the north and south becomes more restricted with depth; equations (15) and (17) give $l_2 = 0.23$ and $l_3 = 0.10$ for the constants of (A6) and $C_1 = -4 \times 10^{-2}$ estimated from the scatter plots. These are realistic estimates of the meridional extent of the homogenized pools in layers 2 and

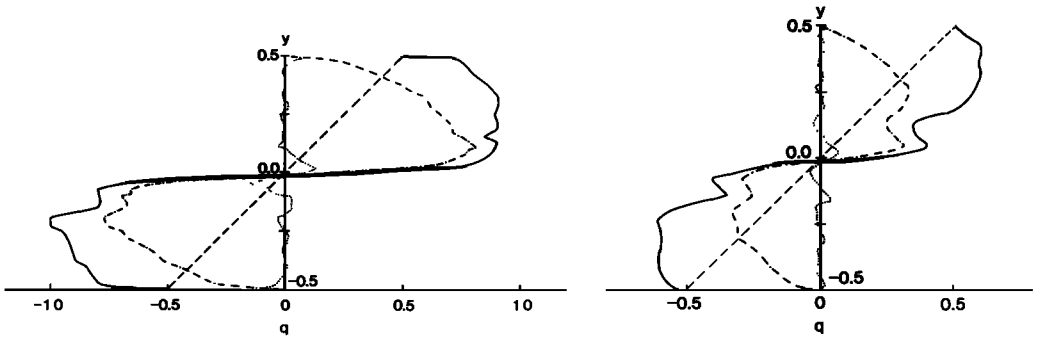

Fig. 8a

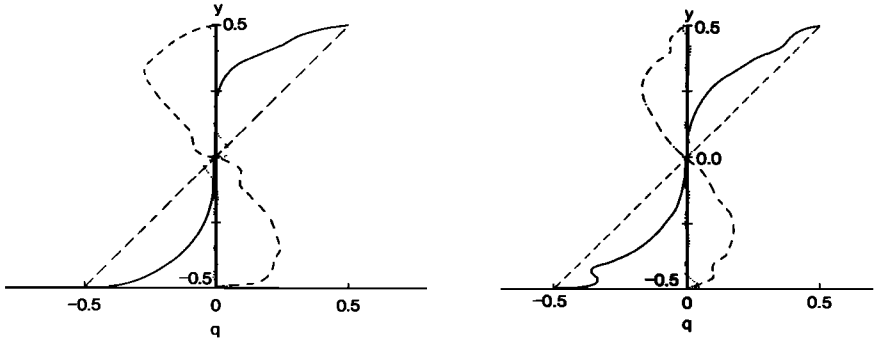

Fig. 8b

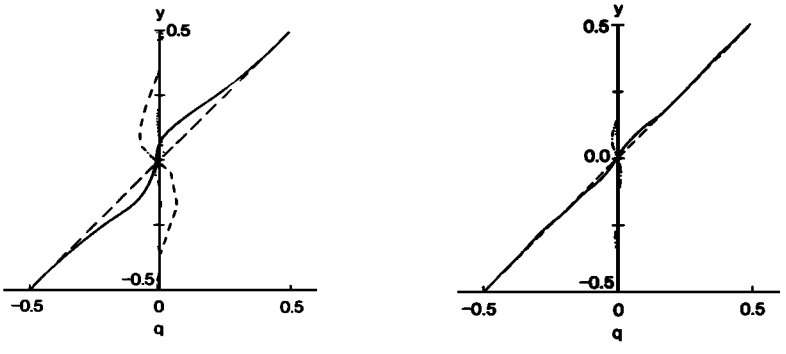

Fig. 8c

Fig. 8. (Left) A meridional section at $x = 1/4$ showing the contribution of planetary vorticity (dashed), relative vorticity (dotted) and stretching (dot-dash) to the time-mean potential vorticity (solid line) of the numerical model fields. (Right) A meridional potential vorticity section for the model fields at $x = 3/4$. (*a*) Layer 1. (*b*) Layer 2. (*c*) Layer 3.

3. The amplitude of the circulation is a strong function of C_1 and, for realistic values, is only weakly dependent upon C_3.

The eastward flowing jet in the upper layer of the numerical model (Figure 1) is well captured but is overemphasized in the inertial limit: the fanning out of the q contours toward their reference latitudes at the east coast is not represented. However, the circulation in layers 2 and 3 is of realistic intensity and meridional scale. The Fofonovian character of the flow in the second and third layers of the numerical model can be seen in Figures 1*b* and 1*c*. Unlike the YR solution, MN predicts flow in the third layer. This barotropic flow, although associated with rather small velocities (typically one tenth of the Sverdrup velocity), extends through the whole depth of the ocean and is responsible for a depth-integrated transport over one half of the Sverdrup transport: 0.56 compared to a Sverdrup transport of 1.0. The remaining 0.84 is carried by the baroclinic homogeneous solution: the baroclinic "fringe" is not weak but carries a substantially greater fraction of the mass transport of the gyre than the barotropic core. The meridional structure of the tight recirculation evident in the barotropic streamfunction computed from the numerical model (see Figure 2) seems to be rather well captured in the inertial theory. Potential vor-

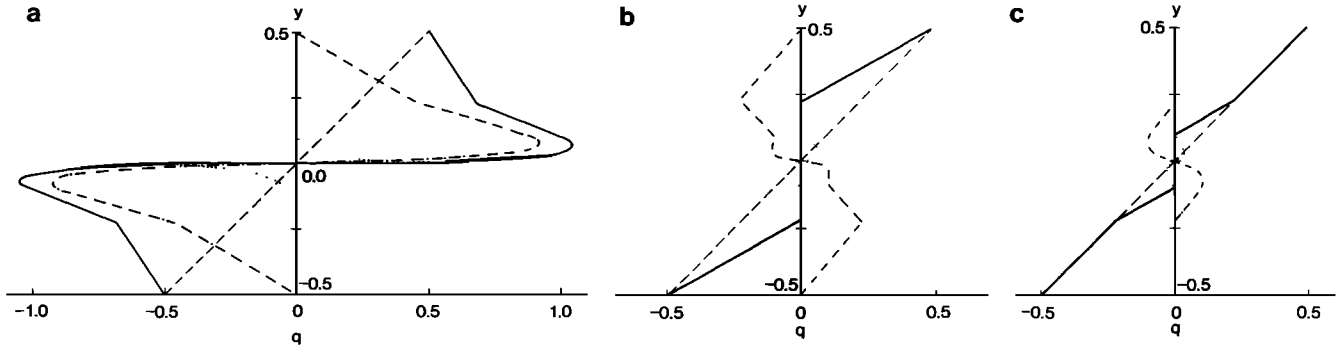

Fig. 9. Meridional potential vorticity sections for the MN solution for (*a*) layer 1, (*b*) layer 2, and (*c*) layer 3. Notation is as in Figure 8.

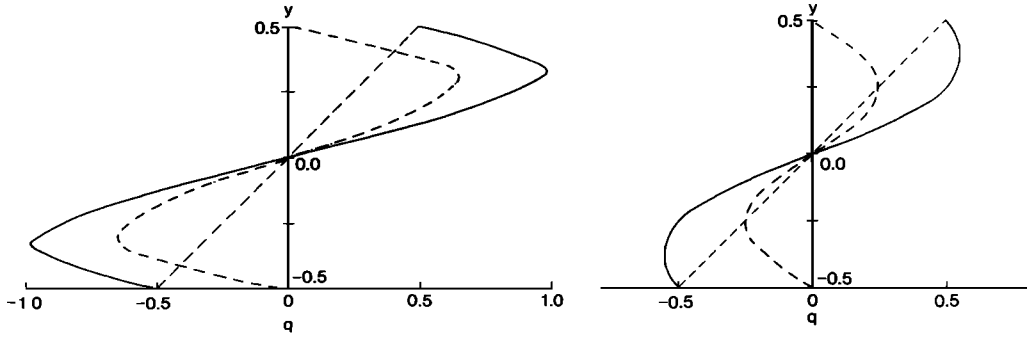

Fig. 10a

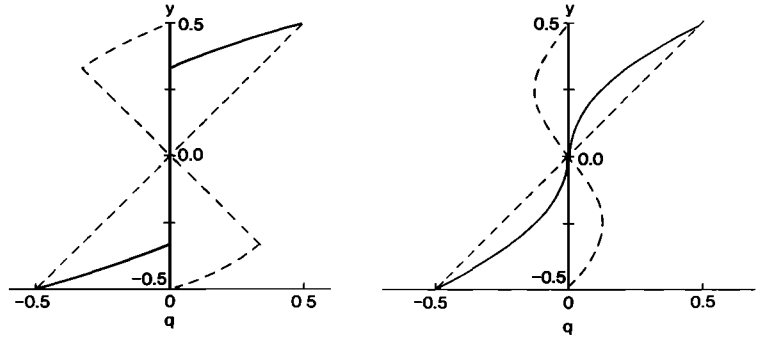

Fig. 10b

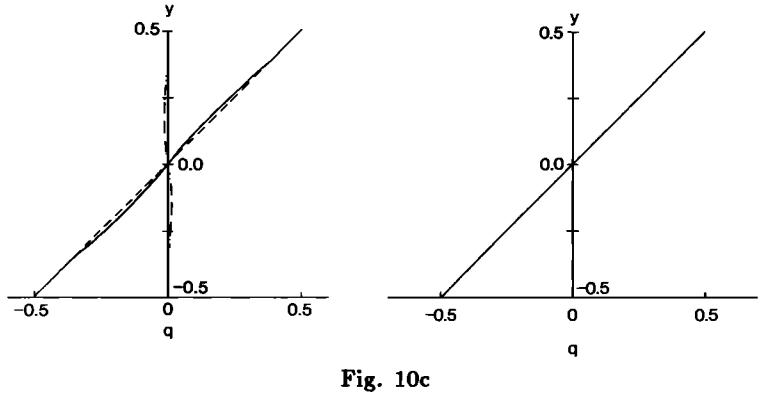

Fig. 10c

Fig. 10. Meridional potential vorticity sections for the YR solution at (left) $x = 1/4$ and (right) $x = 3/4$ for (*a*) layer 1, (*b*) layer 2, and (*c*) layer 3. Notation is as in Figure 8.

ticity budgets described in section 5 show that the relative vorticity makes an important contribution to q in the upper reaches of this tight recirculating gyre. Indeed, it is only because of the presence of inertial boundary layers in the MN model that flow is possible in the deep third layer: closed q contours occur in the third layer because the layer depth changes rapidly in the westerly shear of the Gulf Stream. This cannot happen in the YR model because relative vorticity is neglected and so flow cannot occur in jets.

5. CONCLUSIONS

We conclude our intercomparison of model and theory by presenting meridional sections from the numerical model and the YR and MN solutions. Figure 8 shows sections at $x = 1/4$ and $x = 3/4$ for the mean fields chosen to represent the inertially controlled western and Sverdrupian eastern margin of the basin: q and its component parts, stretching, planetary vorticity and relative vorticity (equation (A2)) are plotted.

In the west ($x = 1/4$) the upper layer exhibits a frontal structure at $y = 0$: note how q decreases (increases) towards the center of the subtropical (subpolar) gyre, consistent with a negative $dq/d\psi$ in the upper layer. Relative vorticity is important in the recirculation most strikingly in the eastward flowing jet at midbasin but also in its tight return flow. In the second layer, q_2 is homogenized over a latitude range extending across both subtropical and subpolar gyres: the front in q evident in the upper layer has disappeared. Relative vorticity again makes an important contribution to the vorticity budget in the recirculation. In the deep third layer velocities are weaker, and flow is confined to a comparatively narrow region about the separated jet at $y = 0$. There is no q front at $y = 0$, but bottom friction prevents the complete homogenization of q. Relative vorticity is still important, even though the flow is weak. These characteristics are rather well captured by the MN solution (see Figure 9).

The meridional sections shown in the left column of Figure 8 seem to support the slippery boundary conditions adopted by the MN model: relative vorticity approaches zero and the potential vorticity is continuous across the edge of the deep recirculating gyre.

The right side of Figure 8 shows a meridional section further east at $x = 3/4$. The YR model (see Figure 10) seems to provide the more relevant reference solution here. At this longitude, inertial effects are less pronounced and gradients less concentrated at midbasin. However, there remains a remnant of the interior jet, but it is no longer intense enough to penetrate down into the lowest layer: q_3 is given by the planetary vorticity as predicted by YR.

Thus the model mean fields exhibit characteristics of both the YR and MN solutions. In the west, where the inertial boundary currents and jets shape the flow, the MN limit is approached; elsewhere, where the Sverdrup constraint holds, the YR solution is more relevant. The YR and MN calculations are best regarded as reference solutions representing analytically tractable and limiting cases which have transparent physics. The numerical model fields lie in between, tending to one or the other depending on model parameters. For example, just as in the barotropic calculations of *Veronis* [1966], a judicious choice of parameters makes it possible (although difficult) to arrange for the separated jet to pentrate right across the basin and approach the inertial limit of MN. Conversely, the separated boundary current can be destabilized by explicit instability and thus inertial effects restricted to a small region of the northwestern corner of the subtropical gyre. In such cases the YR solution describes the flow over the greater part of the domain. Unfortunately, the dependence of the penetration scale on the explicit lateral diffusion, bottom friction, boundary conditions, layer depths and stratification is complicated and not completely understood; see *Holland and Schmitz* [1985] for a model parameter study of the penetration scale of the interior jet. Attempts to control the penetration scale by tuning the lateral friction alone have not been successful.

The problem remains of how to meld the two solutions together. Analytical studies have been carried out which address aspects of this matching problem. For example, *Niiler* [1966] distorts a barotropic Fofonoff gyre, and *Nurser* [1988] a baroclinic Fofonoff gyre by wind forcing, constraining the meridional transport to be in Sverdrup balance. Nurser in particular offers a plausible explanation of the origin of the 'C' observed in the dynamic height reviewed by *Reid* [1982] and evident in our model fields (Figure 1). But how does an eastward flowing inertial boundary current diminish and join on to a Sverdrup interior? In our numerical model, eddy transfer is the agency allowing the ψ and q contours to cross as mean streamlines emerge from the jet to join onto the Sverdrup interior. But in the ocean other processes may also be important: see, for example, *Luyten et. al.* [1987] who consider buoyancy losses. Such processes must undoubtedly be included in more complete theories.

APPENDIX

The potential vorticity equation (nondimensionalized)

$$\frac{1}{R}\frac{\partial q_n}{\partial t} + J(\psi_n, q_n) = G_n \tag{A1}$$

is integrated forward numerically [*Brugge et al.*, 1987] for each level ($n = 1$, 2, or 3) on a finite-difference grid in a square domain, where q_n is the quasi-geostrophic potential vorticity, ψ_n is the streamfunction, G_n is the potential vorticity forcing function, J(a,b) is the Jacobian of a and b, $\partial a/\partial x \partial b/\partial y - \partial b/\partial x \partial a/\partial y$ and x ($0 \le x \le 1$) is east, y ($-0.5 \le y \le 0.5$) is north and t is time.

The potential vorticity is related to the streamfunction through

$$\mathbf{q} = R\nabla^2\mathbf{\Psi} + \mathbf{y} - \underline{\mathbf{S}}\mathbf{\Psi} \tag{A2}$$

where

$$\mathbf{q} = \begin{pmatrix} q_1 \\ q_2 \\ q_1 \end{pmatrix} \qquad \mathbf{\Psi} = \begin{pmatrix} \psi_1 \\ \psi_2 \\ \psi_1 \end{pmatrix}$$

and $\underline{\mathbf{S}}$ is the stretching matrix given by

$$\underline{\mathbf{S}} = \frac{RL^2}{L_T^2}\begin{pmatrix} \frac{1}{\delta_1\Delta\sigma_{21}} & \frac{-1}{\delta_1\Delta\sigma_{21}} & 0 \\ \frac{-1}{\delta_2\Delta\sigma_{21}} & \frac{1}{\delta_2\Delta\sigma_{21}} + \frac{1}{\delta_2\Delta\sigma_{32}} & \frac{-1}{\delta_2\Delta\sigma_{32}} \\ 0 & \frac{-1}{\delta_3\Delta\sigma_{32}} & \frac{1}{\delta_3\Delta\sigma_{32}} \end{pmatrix} = \begin{pmatrix} S_{11} & -S_{12} & 0 \\ -S_{21} & S_{22} & -S_{23} \\ 0 & -S_{32} & S_{33} \end{pmatrix} \tag{A3}$$

In (A1), (A2) and (A3), length has been nondimensionalized with respect to L, where L is the north-south extent of the basin, depth with respect to ocean depth H; time with respect to $(\beta L)^{-1}$ where β is the planetary vorticity gradient; ψ is with respect to $U_S L$, where $U_S = f_o W_{BK}/\beta H$ is a characteristic velocity chosen to be the Sverdrup velocity, f_o is the reference Coriolis parameter, W_{BK} is an Ekman pumping velocity; and q with respect to βL.

The coefficient $R = U_S/\beta L^2$ is a Rossby number for the vorticity equation, $L_T = \sqrt{gH/1000 f_o^2}$ is a pseudo-Rossby radius, $\Delta\sigma_{n+1,n} = 10^3 \Delta\rho_{n+1,n}/\rho_0$ expresses the density jumps between the layers in σ units where

$$\Delta\rho_{n+1,n} = \rho_{n+1} - \rho_n$$

and $\delta_n = H_n/H$ are the fractional layer depths.

The G values in (A1) are given by

$$G_1 = \frac{1}{\delta_1} W_o - \nu \nabla^6 \psi_1 \qquad \text{(A4a)}$$

$$G_2 = -\nu \nabla^6 \psi_2 \qquad \text{(A4b)}$$

$$G_3 = -\nu \nabla^6 \psi_3 - \epsilon \nabla^2 \psi_3 \qquad \text{(A4c)}$$

where W_o is the (nondimensionalized) vertical velocity at the base of the Ekman layer in units of W_{BK}:

$$W_o = \sin 2\pi y \qquad \text{(A5)}$$

The coefficients ν and ϵ are lateral and bottom diffusion constants respectively.

The mean flows presented in Figure 1 were obtained by integrating the model from a state of rest and averaging the fields every 12 days over a 3-year period of the statistically steady state. The model parameters chosen for the integration are

$$H_1 = 500\,\text{m} \qquad \sigma_1 = 27.0 \qquad \text{(A6a)}$$

$$H_2 = 1000\,\text{m} \qquad \sigma_2 = 29.0 \qquad \text{(A6b)}$$

$$H_3 = 3500\,\text{m} \qquad \sigma_3 = 30.0 \qquad \text{(A6c)}$$

$L = 3\text{x}10^6$ m, $\beta = 10^{-11}\,\text{m}^{-1}\,\text{s}^{-1}$, $f_o = 7\text{x}10^{-5}\,\text{s}^{-1}$, $U_S = 2\text{x}10^{-3}\,\text{m s}^{-1}$ giving $R = 2\text{x}10^{-5}$ and $L_T = 70$ km; and coefficients of the stretching matrix (equation (A3)) of magnitude

$$\underline{\mathbf{S}} = \begin{pmatrix} 10 & -10 & 0 \\ -5 & 15 & -10 \\ 0 & -2.85 & 2.85 \end{pmatrix} \times 10^{-2}$$

The above imply internal Rossby radii of 48 and 18 km.

Acknowledgments. We gratefully acknowledge the use of computing facilities of the European Centre for Medium Range Weather Forecasts which made this study possible. Thanks are due also to D. R. Moore of Imperial College, who made available his extremely rapid elliptic equation solvers and to D. Haidvogel who advised on parameter regimes for the model. The Natural Environment Research Council provided support for A.J.G.N.

REFERENCES

Brugge, R., A. J. G. Nurser, and J. C. Marshall, A quasi-geostrophic ocean model, internal report, *61* pp., Imp. Coll., London, 1987.

Bryan, K., A numerical investigation of a nonlinear model of a wind-driven ocean, *J. Atmos. Sci.*, *20*, 594–606, 1963.

Cessi, P., G. R. Ierley, and W. R. Young, A model of the inertial recirculation driven by potential vorticity anomalies, *J. Phys. Oceanogr.*, *17*, 1640–1652, 1987.

Fofonoff, N. P., Steady flow in a frictionless homogenous ocean, *J. Mar. Res.*, *13*, 254–262, 1954.

Holland, W. R. and W. J. Schmitz, Zonal penetration scale of model midlatitude jets, *J. Phys. Oceanogr.*, *15*, 1859–1875, 1985.

Ierley G. R. and W. R. Young, Can the western boundary layer affect the potential vorticity distribution in the Sverdrup interior of a wind gyre?, *J. Phys. Oceanogr.*, *13*, 1753–1763, 1983.

Luyten, J. R., N. Hogg, and H. Stommel, Closing the oceanic circulation, *Deep Sea Res.*, *34*, 55–60, 1987.

Marshall J. C. and A. J .G. Nurser, Steady free circulation in a stratified quasi-geostrophic ocean, *J. Phys. Oceanogr.*, *16*, 1799–1813, 1986.

Marshall J. C. and A. J. G. Nurser, On the recirculation of the subtropical gyre, *Q. J. R. Meteorol. Soc.*, in press, 1988.

Niiler, P. P., On the theory of the wind-driven ocean circulation, *Deep Sea Res.*, *13*, 597–606, 1966.

Nurser, A. J. G., The distortion of a baroclinic Fofonoff gyre by wind forcing, *J. Phys. Oceanogr.*, *18*, 243–257, 1988.

Read, P. L., P. B. Rhines, and A. A. White, Geostrophic scatter diagrams and potential vorticity dynamics, *J. Atmos. Sci.*, *43*, 3226–3240, 1986.

Reid, J. L., On the mid-depth circulation of the world ocean, in *Evolution of Physical Oceanography*, edited by B. A. Warren and C. Wunsch, MIT Press, Cambridge, Mass., 1982.

Rhines, P. B. and W. R. Young, A theory of the wind-driven circulation. I. Mid-ocean gyres, *J. Mar. Res.*, *40*, 559–596, 1982.

Schmitz, W. J., Weakly depth-dependent segments of the North Atlantic circulation, *J. Mar. Res.*, *38*, 111–133, 1980.

Schmitz, W. J. and W. R. Holland, Observed and modeled mesoscale variability near the Gulf Stream and Kuroshio extension, *J. Geophys. Res.*, *91*, 9624–9638, 1986.

Stommel, H., The westward intensification of wind-driven ocean currents, *Eos Trans. AGU*, *29*, 202–206, 1948.

Veronis, G., Wind-driven ocean circulation: Part I. Numerical solutions of the non-linear problem, *Deep Sea Res.*, *13*, 31–55, 1966.

Young, W. R and P. B. Rhines, A theory of the wind-driven circulation. II. Gyres with western boundary currents, *J. Mar. Res.*, *40*, 849–872, 1982.

R. Brugge, J. C. Marshall, and A. J. G. Nurser, Space and Atmospheric Physics Group, Department of Physics, Imperial College, Blackett Laboratory, Prince Consort Road, London SW7 2BZ, England.

(Received October 13, 1987;
revised July 7, 1988;
accepted July 11, 1988.)